frontiers | Frontiers in Chemistry

TYPE Original Research
PUBLISHED 06 November 2024
DOI 10.3389/fchem.2024.1478560

Check for updates

OPEN ACCESS

EDITED BY
Zhao Jiang,
Xi'an Jiaotong University, China

REVIEWED BY
Ivaylo Tankov,
Prof. Assen Zlatarov University, Bulgaria
Wen Luo,
Shanghai University, China

*CORRESPONDENCE
Wuguo Wei,
weiwuguo@163.com
Xing Peng,
372913156@qq.com

†These authors have contributed equally to this work and share first authorship

RECEIVED 10 August 2024
ACCEPTED 21 October 2024
PUBLISHED 06 November 2024

CITATION
Zhang J, Wu C, Wang J, Xia M, Li S, Liu L, Wei W and Peng X (2024) DFT-guided synthesis of N, B dual-doped porous carbon from saccharina japonica for enhanced oxygen reduction catalysis.
Front. Chem. 12:1478560.
doi: 10.3389/fchem.2024.1478560

COPYRIGHT
© 2024 Zhang, Wu, Wang, Xia, Li, Liu, Wei and Peng. This is an open-access article distributed under the terms of the Creative Commons Attribution License (CC BY). The use, distribution or reproduction in other forums is permitted, provided the original author(s) and the copyright owner(s) are credited and that the original publication in this journal is cited, in accordance with accepted academic practice. No use, distribution or reproduction is permitted which does not comply with these terms.

DFT-guided synthesis of N, B dual-doped porous carbon from saccharina japonica for enhanced oxygen reduction catalysis

Junjie Zhang†, Chao Wu†, Jilong Wang, Maosong Xia, Shixin Li, Long Liu, Wuguo Wei* and Xing Peng*

College of Aeronautical Engineering, Civil Aviation Flight University of China, Chengdu, China

Introduction: The oxygen reduction reaction (ORR) is a crucial determinant of the energy transformation capacity of fuel cells. This study investigates the performance of N and B dual-doped carbon in ORR.

Methods: Six models using density functional theory (DFT) are developed to compare the performance of different doping strategies. A highly efficient dual-doped carbon ORR catalyst (S-850-1) is synthesized from *Saccharina japonica*, containing 4.54 at% N and 1.05 at% B atom.

Results: Electrochemical analysis reveals that S-850-1 significantly outperforms the nitrogen mono-doped carbon S-850, exhibiting a higher half-wave potential of 0.861 V and a greater limited current density of −5.60 mA cm^{-2}, compared to S-850's 0.838 V and −5.24 mA cm^{-2}. Furthermore, S-850-1 surpasses the performance of 20% Pt/C, demonstrating enhanced durability and exceptional resistance to CO and methanol. The 1.40 V open circuit voltage produced by S-850-1 when integrated into a Zn-air battery can power an LED light.

Discussion: Both theoretical and practical evaluations validate the excellent ORR performance of nitrogen and boron dual-doped carbon, as evidenced by the agreement between the electrochemical results and DFT calculations. This work not only extends the range of ORR catalysts derived from biomass but also provides guidance on creating and producing affordable, effective catalysts that utilize natural resources.

KEYWORDS

ORR, DFT, N and B dual-doping carbon, fuel cell, biomass

1 Introduction

Fuel cells (FCs) are particularly important due to their potential for integration into the hydrogen cycle (Hren et al., 2021; Mao et al., 2022). FCs are an innovative technology that efficiently and quietly converts chemical energy into electricity, offering significant ecological benefits. Their vast potential spans applications in small electronic devices, civil aviation, and aerospace equipment (Xiao et al., 2021). The oxygen reduction process is the main element influencing FCs' energy conversion efficiency (ORR). Platinum (Pt), a noble metal, is considered the best catalyst for ORR (Su et al., 2021). The performance of the ORR catalyst is crucial for the efficiency of FCs (Arif et al., 2024). However, the limited durability, high-cost, and vulnerability to CO and methanol poisoning of Pt, along with its

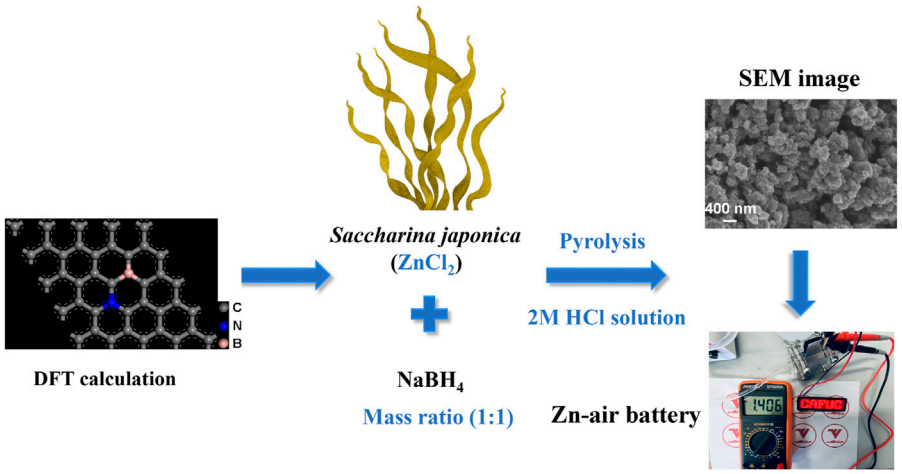

SCHEME 1
The synthesis process of N and B dual-doping carbon ORR catalyst derived from saccharina japonica.

restricted global supply, hinder its economic feasibility (Liu et al., 2024). As a result, many researchers are investigating substitute catalysts, including low precious metal alloy catalysts, heteroatom-doped carbon catalysts, and transition metal-based catalysts (Bhoyate et al., 2023). Heteroatom doping carbon ORR catalysts have attracted a lot of attention because of their improved activity, extended stability, and outstanding resistance to methanol and CO (Gu et al., 2018).

Common heteroatoms used include boron (B), sulfur (S), phosphorus (P), and nitrogen (N) (Choi et al., 2013; Ferrero et al., 2016; Choi et al., 2012; Yang et al., 2012; Zhao et al., 2017; Cai et al., 2019). These heteroatoms may alter the electron distribution in nearby carbon atoms, improving oxygen molecule adsorption, reduction, and desorption, due to their different electronegativities from carbon (Zheng et al., 2012; Higgins et al., 2014). In contrast, biomass-derived carbon catalysts doped with heteroatoms offer several inherent advantages, including an abundant supply of natural heteroatoms, lower synthesis costs, and environmental sustainability (Borghei et al., 2018; Wang et al., 2020). Research indicates that carbon materials from biomass sources such as water hyacinth, soybean, okara, bamboo fungus, and grape skin are often mono-nitrogen doped (Liu et al., 2015; Guo et al., 2015; Gao et al., 2014a; Gao et al., 2014b; Chen et al., 2014; Alatalo et al., 2016; Zhao et al., 2018; Zhang et al., 2023a; Huang et al., 2020). Few studies have investigated carbon derived from biomass with dual heteroatom doping, with most research focusing on N and S dual doping in materials such as feathers, seaweed, chrysanthemum, and honeysuckle (Liu et al., 2014; Xu et al., 2017; Gao et al., 2015a; Gao et al., 2015b). Compared to single heteroatom doping, introducing multiple types of heteroatoms can further increase the asymmetry of carbon atoms' spin and charge density, potentially enhancing ORR performance (Huang et al., 2020). Additionally, external boron doping in N-doping carbon has been demonstrated to further improve ORR performance (Wei et al., 2021). For instance, the current density and half-wave potential of B doping N doped carbon have been reported to increase from −0.23 to −0.21 V and from −5.26 to −5.64 mA cm^{-2}, respectively (Huang et al., 2017; Zeng et al., 2020). Few studies have focused on biomass-derived dual heteroatom-doped carbon catalysts, with most previous research emphasizing the synthesis of N and B dual-doping carbon using chemical precursors (Lee et al., 2016; Li et al., 2022). Developing a dual-doped carbon ORR catalyst from biomass could present a strong candidate for commercial applications, offering distinct advantages: high ORR activity, cheap, sustainability, and environmental friendliness.

The brown algae saccharina japonica (phylum phaeophyta) is rich in protein, with content ranging from 6.8% to 10.3%, and serves as both a food source and a valuable source of heteroatoms (Xu et al., 2014; Su et al., 2022). Proteins, which are predominantly composed of nitrogen-rich amino acids, are the primary contributors of nitrogen. Boron is sourced from $NaBH_4$. This study examines the efficiency of N and B dual-doping carbon using DFT calculations. Saccharina japonica is rich in N element, and $NaBH_4$ serves as a source of both B and N atoms. Through high-temperature pyrolysis, dual-doped carbon materials containing N (4.54 at%) and B (1.05 at %) are produced. S-850-1, the synthesized sample, has a better limited current density (−5.60 mA cm^2) and half-wave potential (0.861 V) than N-doping carbon (S-850: 0.838 V and −5.24 mA cm^2). S-850-1 shows promise as ORR catalyst in FCs, considering the abundance of saccharina japonica worldwide and the rarity of N, B dual-doping carbon generated from biomass.

2 Experimental

2.1 Materials

Saccharina japonica is cleaned with water, and then baked to dryness. After being dried and powdered into a fine powder (5 g), 10 g $ZnCl_2$ and 500 mL water are combined, and the above mixture are constantly agitated for 48 h. Above mixture is baked in an oven (80°C) until a fully dry colloid form. This colloid undergoes pyrolysis into a quartz at 850°C for 2 h. Above carbon material is combined with $NaBH_4$ at a 1:1 mass ratio. The heated material is washed repeatedly with 2 M HCl solution and water until it reaches a neutral pH. The final product is labeled S-850-1. The sample, prepared using the same method as described above without the addition of $ZnCl_2$,

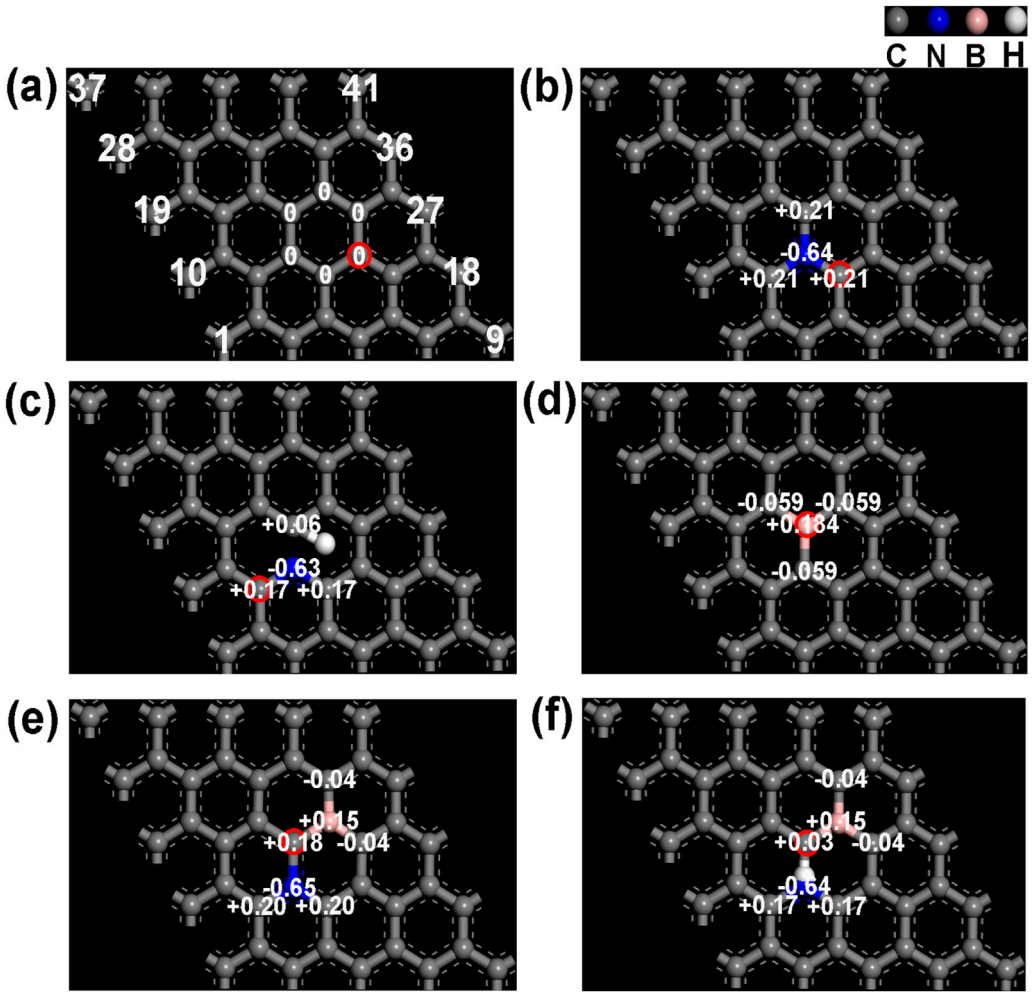

FIGURE 1
(A) Graphene, **(B)** graphitic-N doped carbon, **(C)** pyridinic-N doped carbon, **(D)** B doped carbon, **(E)** graphitic-N, B dual doped carbon, and **(F)** pyridinic-N, B dual doped carbon's charge distribution images.

is designated as SN-850-1. The pyrolysis temperature of the samples is increased from 850°C to 1,000°C, with holding times of 2 and 3 h, respectively, denoted as S-1000-2 and S-1000-3. S-1000-2 is mixed with $NaBH_4$ in a 1:1 ratio, with the pyrolysis temperature set at 850°C and held for 2 h, resulting in the sample being named S-850-B.

2.2 DFT calculations

The population analysis, electron density difference, and adsorption free energy of O*, OH*, and OOH* (descriptors) are calculated using VASP software. The exchange-correlation functional is set to GGA-PBE. The energy cutoff for the plane-wave basis set is 500 eV, and the projector augmented wave method is used for pseudopotentials. A solvation model is applied using implicit solvation, and the dielectric constant for water (H_2O) is set to 78.5. The slab model is based on a graphene structure with a (4 × 4 × 3) supercell, with the bottom two layers of the slab fixed during relaxation. A vacuum layer of 20.0 Å is included, and the cleave plane is oriented along the (002) direction.

2.3 Characterization

D/MAX-Ultima + diffractometer with Co. Kα radiation is used for XRD. Using a WBL-810 apparatus, N_2 adsorption-desorption tests are carried out at 77 K. The microstructural morphology of the produced samples is examined with a Supra-55 sapphire fitted FE-SEM.

2.4 Electrochemical measurements

The electrochemical studies are done using a Corrtest CS310 M electrochemical station. Following a combination of 10 mg sample, 5 mL isopropanol, and 20 μL 5% Nafion, the mixture underwent a 20 min ultrasonography treatment. Experiments using LSV (linear sweep voltammetry) and CV (cyclic voltammetry) are conducted at scan speeds of 10 and 20 mV s^{-1}, respectively. At rotating speeds from 400 to 2,500 rpm, LSV curves are recorded in alkaline electrolyte.

To get the transferred electron number (N), the Koutechy-Levich (K-L) curve's slope is calculated using Equations 1, 2.

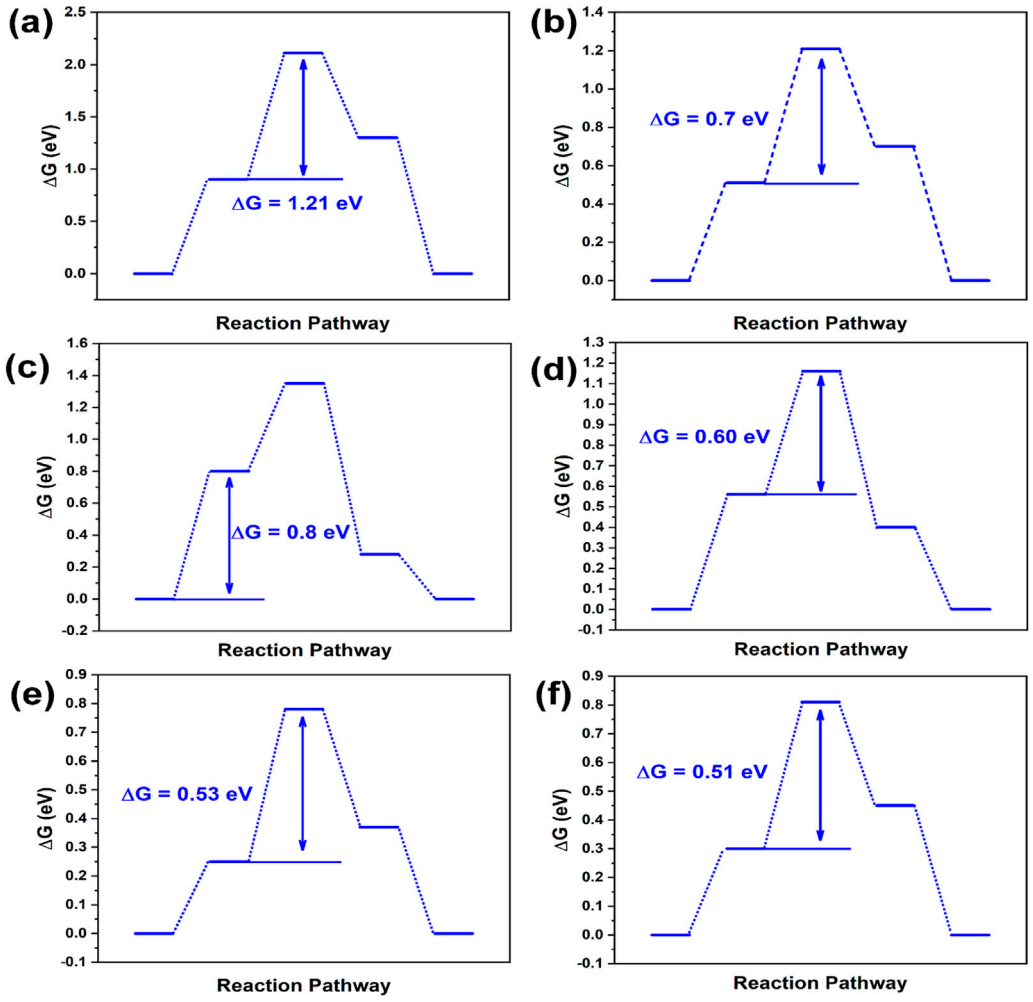

FIGURE 2
Energy step images of **(A)** graphene, **(B)** graphitic-N doped carbon, **(C)** pyridinic-N doped carbon, **(D)** B doped carbon, **(E)** graphitic-N, B dual doped carbon, and **(F)** pyridinic-N, B dual doped carbon.

$$\frac{1}{J} = \frac{1}{J_L} + \frac{1}{J_K} = \frac{1}{B\omega^{1/2}} + \frac{1}{J_K} \quad (1)$$

$$B = 0.2nFC_0D^{2/3}\nu^{-1/6} \quad (2)$$

The current density measured during the electrochemical experiments is denoted as J, while J_k represents the kinetic current density and J_L corresponds to the limited current density. n is the representation of the transmitted electron number. B represents the Levich slope, and the electrode rotating rate is indicated by ω. The Faraday constant, denoted as F. The diffusion coefficient of O_2 is represented as D, and the bulk concentration of O_2 is denoted as C. v is the kinetic viscosity representation.

3 Results and discussions

3.1 Model design

This study uses DFT calculations to confirm that the ORR activity of the N, B dual-doping carbon model is higher than that of the N or B mono-doping carbon models. Saccharina japonica and $NaBH_4$ are employed as sources of N and B, respectively. High-temperature pyrolysis and washing with 2 M HCl solution are then applied to produce carbon materials doped with N (4.54 at%) and B (1.05 at%) as shown in Scheme 1.

Reports commonly identify graphitic and pyridinic nitrogen as the most effective active sites for ORR (Guo et al., 2020; Liang and Yuan, 2024). Figures 1, 2 depict reaction energy barriers and the charge distribution for models of graphene, pyridinic-N, graphitic-N, and B-doping carbon. The O*, OH*, and OOH* species exhibit favorable adsorption and desorption energies, as shown by their adsorption at the reaction sites marked by red circles in these models. The graphene model demonstrates a homogeneous charge distribution, as seen in Figures 1A, 2A, leading to a substantial energy barrier for the reaction (1.21 eV in step 2) and limited adsorption capacity. As shown in Figure 1B, graphitic-N (N_{13}) is bonded to three carbon atoms (C_{12}, C_{14}, C_{23}), forming three C-N bonds. The electronegativity of N atom (3.04) is higher than that of C atom (2.55), causing the N atom to attract the valence electrons of the C atoms. As a result, N atom accumulates electrons,

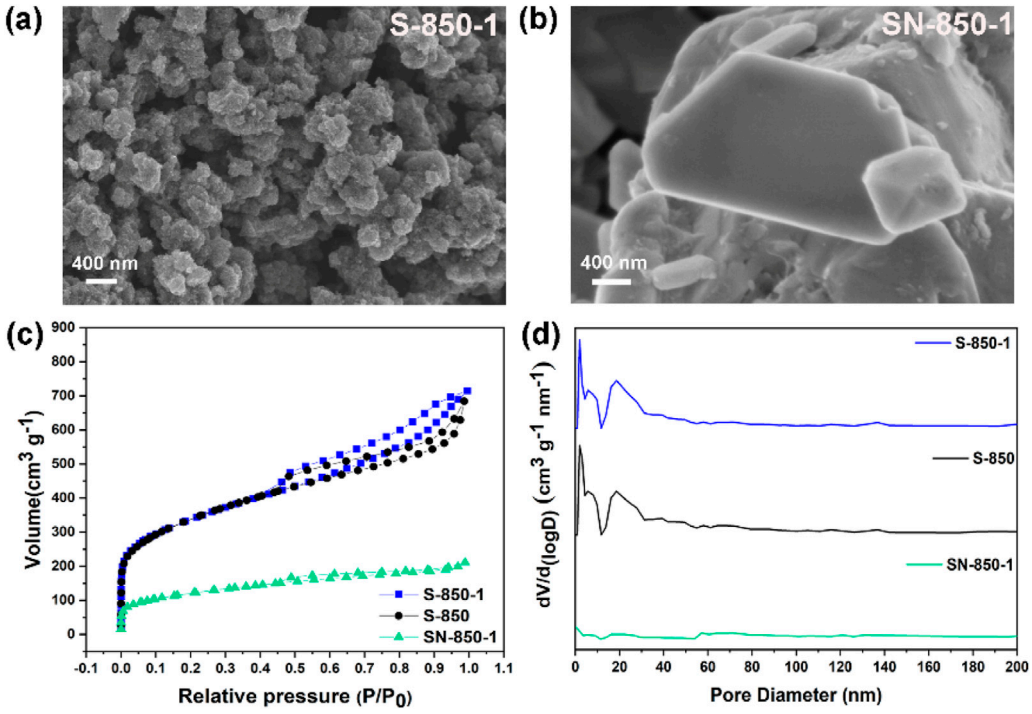

FIGURE 3
(A, B) SEM images of S-850-1 and SN-850-1, **(C, D)** N_2 adsorption-desorption isotherms and pore size of the as-synthesized samples.

gaining a charge of −0.64 e, while the three surrounding C atoms (C_{12}, C_{14}, C_{23}) lose valence electrons, each acquiring a charge of +0.21 e. The reaction energy barrier of the graphitic-N doped carbon model is reduced to 0.70 eV in step 2 (Figure 2B), attributed to the uneven distribution of the electron cloud.

In Figure 1C, the pyridinic-N atom forms C-N bonds with two carbon atoms (C_{12} and C_{14}). Due to the presence of a lone pair of electrons, pyridinic-N exhibits a weaker electron-attracting ability compared to graphitic-N. Consequently, C_{12} and C_{14} carry a charge of +0.17 e, while C_{23} exhibits a charge of +0.06 e. Due to the uneven electron cloud distribution, the reaction energy barrier of pyridinic-N doped carbon is reduced to 0.80 eV (step 1) in Figure 2C.

Electronegativity of B atom (2.04) is lower than that of C atom, causing its electrons to be attracted by the surrounding C atoms (C_{13}, C_{22}, and C_{24}). B atom carries a charge of +0.184 e, while the neighboring C atoms (C_{13}, C_{22}, and C_{24}) carry a charge of −0.059 e in Figure 1D. The reaction energy barrier of B-doped carbon is further reduced to 0.60 eV (step 2) in Figure 2D. In Figure 1E, the dual doped graphitic-N and B atoms further disrupts the electron cloud distribution. The electron density of graphitic-N atom increases to −0.65 e, while the electron density of B atom decreases to +0.15 e. The surrounding carbon atoms, C_{12} and C_{14}, carry a charge of +0.20 e, C_{23} carries +0.18 e, while C_{25} and C_{34} carry −0.04 e. These changes in electron distribution are attributed to the coupling effect between the graphitic-N and B atoms. In Figure 2E, the reaction energy barrier of graphitic-N and B doped carbon is further reduced to 0.53 eV in step 2. Similarly, pyridinic-N and B dual doping also further disrupts the electron distribution in the carbon structure. The electron density of pyridinic-N atom increases to −0.64 e, while the electron density of B atom decreases to +0.15 e. The surrounding carbon atoms, C_{12} and C_{14}, carry a charge of +0.17 e, C_{23} carries +0.03 e, while C_{25} and C_{34} carry −0.04 e. In Figure 2F, the reaction energy barrier of graphitic-N and B doped carbon is further reduced to 0.51 eV in step 2. According to the DFT calculation results, the graphitic-N, pyridinic-N and B dual-doped carbon structure further disrupts the electron cloud distribution, adjusts the adsorption energies of intermediate species O*, OH*, and OOH*, thereby lowering the energy barrier for the ORR, which is beneficial for enhancing ORR catalytic performance.

3.2 Physical characterization

DFT findings suggest that N, B dual-doping carbon may exhibit exceptional ORR performance. N, B dual-doping carbon ORR catalysts are synthesized from saccharina japonica.

SEM pictures provide visual information on the shape and structure of the as-synthesized samples. In Figure 3A, S-850-1 exhibits a porous surface morphology, with interconnected carbon particles forming the surface porosity. The porous morphology enhances the exposure of active sites and improves O_2 molecule transport. As shown in Figure 3B, SN-850-1 demonstrates a large, solid bulk structure at the micrometer scale, with a non-porous surface. SEM analysis indicates that the porous structure of the sample is attributed to the influence of $ZnCl_2$ activator. N_2 adsorption-desorption study assesses the surface area and distribution of pore sizes. In Figure 3C, mesopores are evident, with both S-850 and S-850-1 exhibiting type-IV isotherms and a distinct hysteresis loop in the medium and high-pressure regions (Wang et al., 2011). However, SN-850-1 exhibits a type II isotherm,

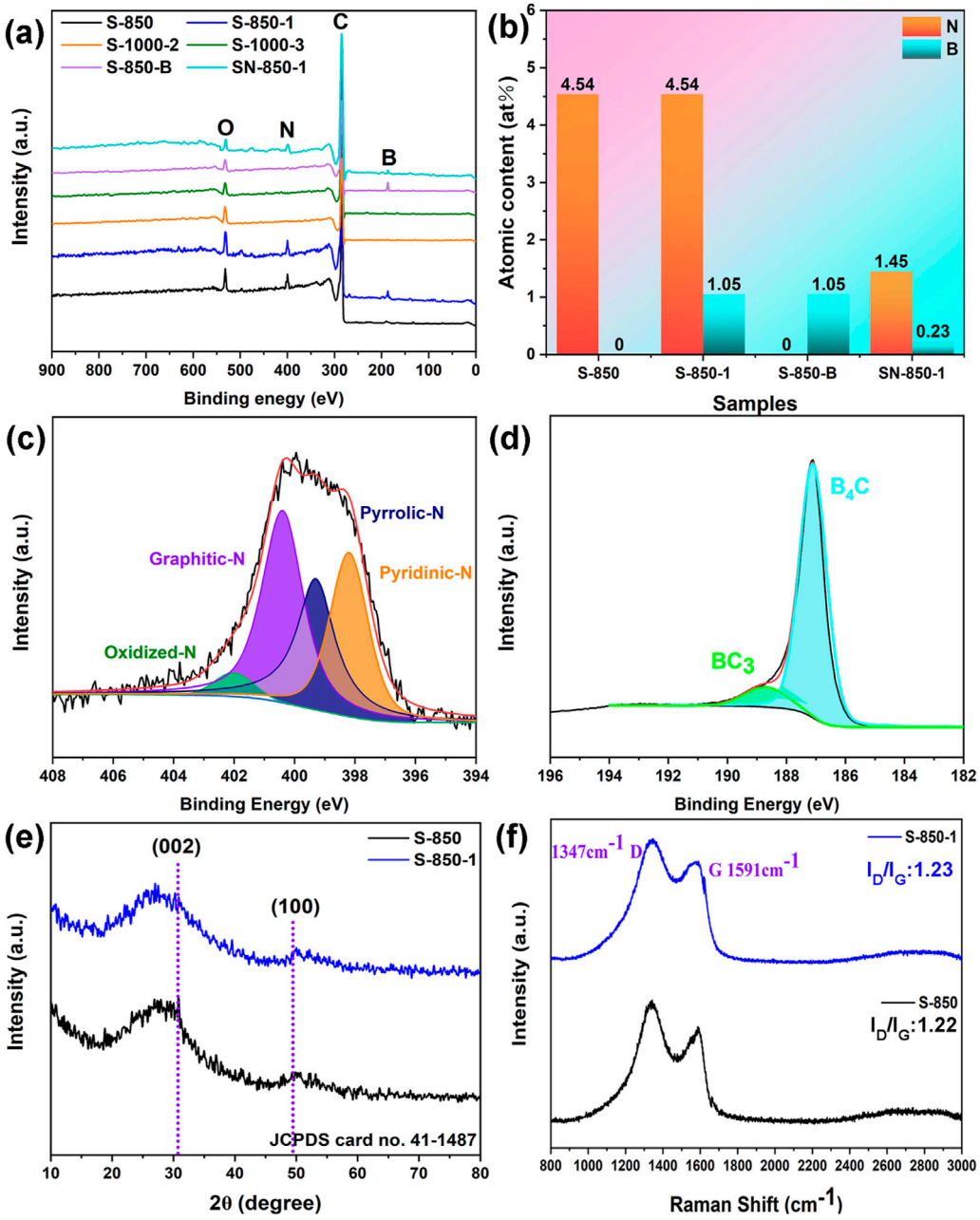

FIGURE 4
(A) Full-scan XPS, **(B)** Total N and B content, **(C, D)** High-resolution N and B atoms of S-850-1, **(E)** XRD pattern, **(F)** Raman spectrum.

indicating a non-porous structure (Li et al., 2019). After doping with B, S-850-1 shows a modest increase in specific surface area from 1,108 to 1,173 m^2 g^{-1}, which is likely attributable to the B atomic incorporation. SN-850-1 exhibits a comparatively low specific surface area of 89 m^2 g^{-1}. Non-local density functional theory, the distribution of pore size shown in Figure 3D is predominantly in the 15–50 nm range, indicating the presence of mesopores. SN-850-1 is characterized by a non-porous structure. Based on the above physical characteristics, $ZnCl_2$ activator is identified as a key factor in the development of the porous structure of biomass-derived carbon-based ORR catalyst, potentially impacting ORR performance.

XPS measurements can be used to analyze the types and quantities of doping N and B atoms. Figure 4A reveals the presence of doped N atoms through peaks at approximately 187 eV (B), 284 eV (C), 532 eV (O), and 400 eV (N) for the as-synthesized samples (Lee et al., 2016). S-850 contains only doped C, O, and N atoms, whereas S-850-1 exhibits significant B doping, confirming the incorporation of B atoms into the N-doped carbon matrix. S-850-1 shows a higher O content than N and B. The pyrolysis temperature of the samples is increased to 1,000°C and maintained for 2 h to ensure the complete volatilization of doped N atom. S-1000-2 is mixed with $NaBH_4$ in a 1:1 ratio, with the pyrolysis temperature set at 850°C and held for 2 h, resulting in the sample being named S-850-B.

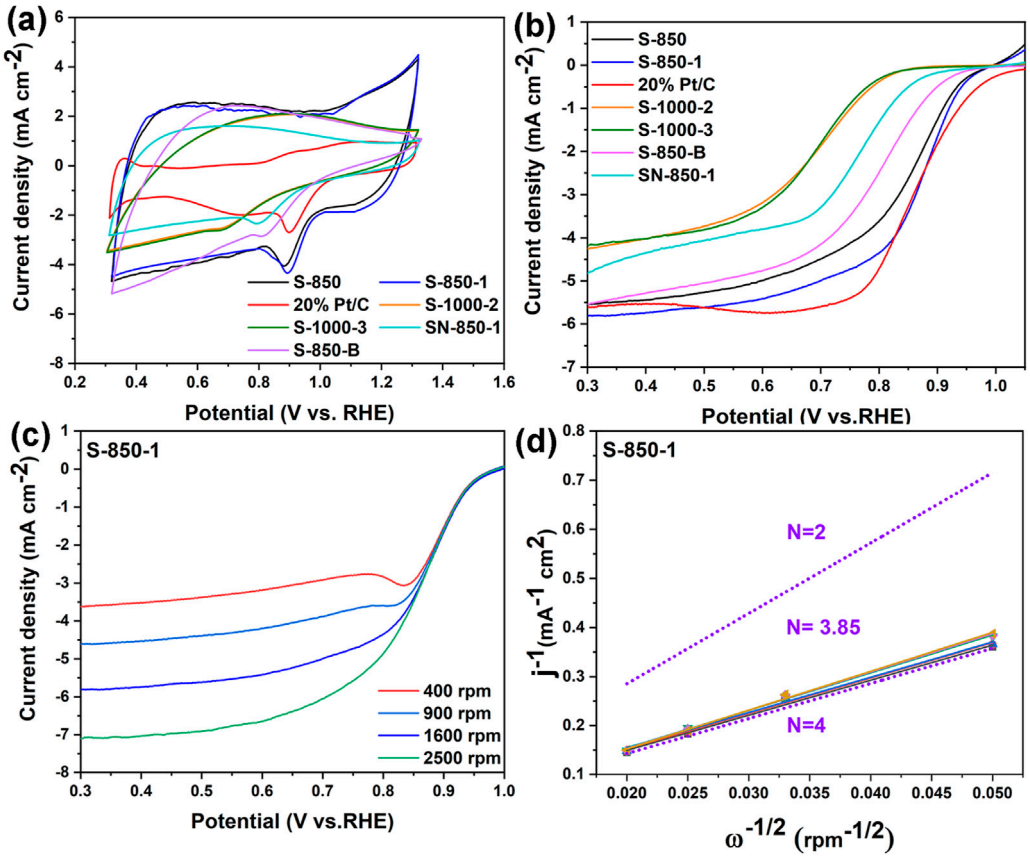

FIGURE 5
(A, B) CV, LSV curves of the as-synthesized samples, **(C)** RDE curves, **(D)** K-L plots of S-850-1.

TABLE 1 Electrochemical characterizations of the as-synthesized samples and previously reported N, B-doped carbon catalysts.

Samples	Peak potential (V)	Onset potential (V)	Half-wave potential (V)	Limited current density @0.5V (mA cm^{-2})
S-850	0.881	0.912	0.838	−5.24
S-850-1	0.895	0.962	0.861	−5.60
20% Pt/C	0.899	1.050	0.862	−5.60
S-850-B	0.805	0.976	0.785	−5.04
SN-850-1	0.795	0.935	0.768	−4.10
S-1000-2	0.682	0.890	0.640	−3.76
S-1000-3	0.682	0.890	0.641	−3.78
BN-GNRs (Tu et al., 2022)	0.870	0.954	0.852	−4.00
B-NHMC (Al-Enizi, 2022)	0.881	0.975	0.835	−4.20
BNC-600 (Zhou et al., 2021)	0.759	0.930	0.790	−5.10

Pyrolysis at 1,000°C, with hold times of 2 and 3 h (noted as S-1000-2 and S-1000-3), is conducted to fully volatilize N and B, aiming to investigate the effect of doped O atom on ORR performance. In the S-1000-2 and S-1000-3 samples, N and B are indeed absent, with only O remaining, which is attributed to the volatilization of N and B at high temperatures. The O contents of S-1000-2 and S-1000-3 are 5.34 at% and 3.21 at%, respectively. Subsequent electrochemical performance tests will be conducted to analyze the effect of doped O atom on ORR performance. N (1.45 at%) and B (0.23 at%) contents in SN-850-1 are lower than

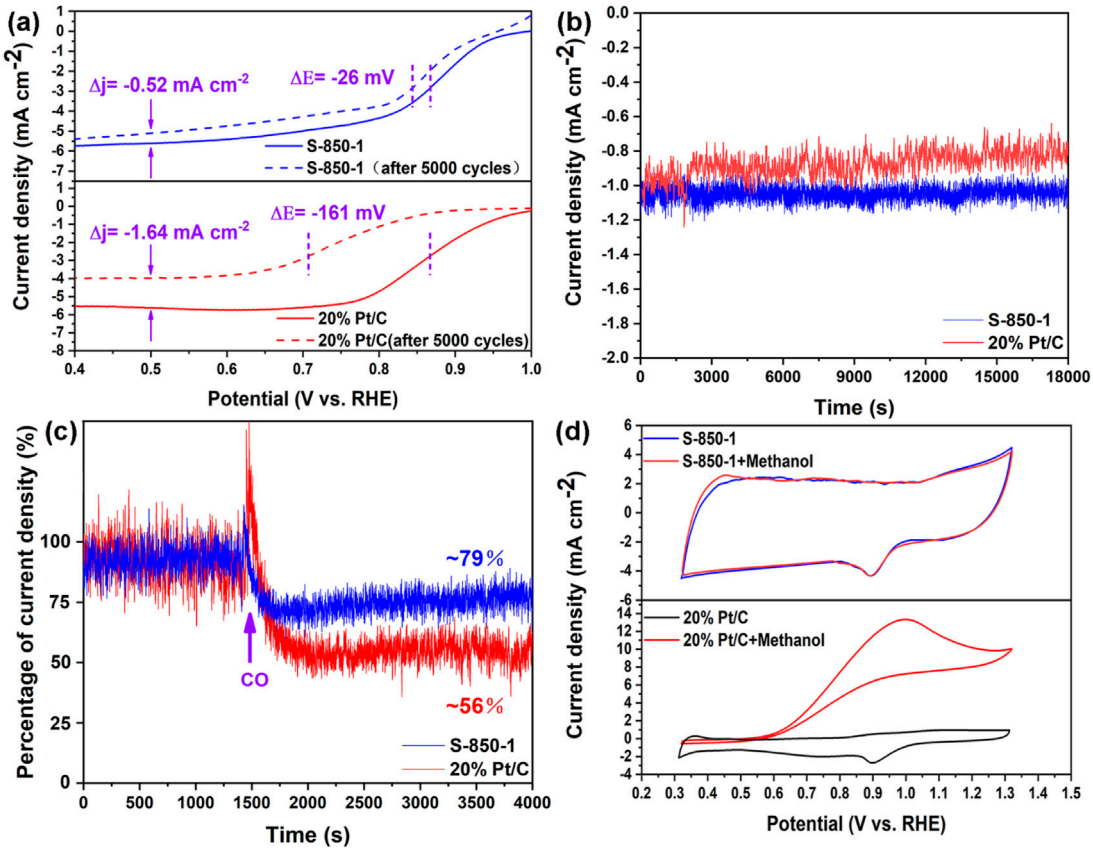

FIGURE 6
(A) LSV curves pre- and post-5000 CV cycles, **(B)** Chronoamperometric measurements, **(C)** Chronoamperometric measurements are obtained, with the inflection point indicating the introduction of CO, **(D)** CV curves in solution and in the presence of methanol.

those in S-850-1 (N: 4.54 at% and B: 1.05 at%), indicating that the porous structure facilitates the exposure of more heteroatoms. Figure 4B shows doping N and B atomic content of the as-synthesized samples. The high-resolution N_{1s} spectra of S-850-1 reveal peaks corresponding to graphitic-N (401 eV), pyridinic-N (398 eV), pyrrolic-N (399 eV), and oxidized-N (402 eV) (Zhang et al., 2023b; Huang et al., 2019). The doped B atoms are represented by peaks at 187 eV (B_4C) and 189 eV (BC_3) in Figures 4C, D. According to the XPS results, saccharina japonica may serve as a precursor for the synthesis of N mono-doping carbon materials. Additionally, combining saccharina japonica with $NaBH_4$ enables the effective production of N and B dual-doping carbon, which may show promising activity for ORR.

XRD patterns of S-850-1 and S-850 exhibit two distinct peaks at $2\theta = 30.7^{\circ}$ and 49.4°, which match to the (002) and (100) crystallographic planes of a standard hexagonal carbon structure (JCPDS card no. 41–1,487) in Figure 4E (Yu et al., 2014). The diffraction peaks of the (002) plane in S-850 and S-850-1 show a slight negative shift relative to the standard peak, indicating that the diffraction is performed by ions (N, and B) of different radius or the defects formed due to incorporation of N or B. Both S-850 and S-850-1 display D and G bands in Raman spectra (Figure 4F). The extent of disorder in the carbon material is reflected in the I_D/I_G ratio of these bands (Kim et al., 2011). For S-850-1, the I_D/I_G ratio is 1.23, showing a slight increase compared to the N mono-doped S-850, which has an I_D/I_G ratio of 1.22. This increases likely results from the enhanced defect density due to B doping.

3.3 Electrochemical characterization

This work assessed the ORR performance of the as-synthesized samples and 20% Pt/C using CV and LSV tests in 0.1 M KOH electrolyte, with recorded potentials plotted against the RHE scale. Figure 5A shows clear reduction peaks for the above samples, demonstrating their ORR activity in an alkaline electrolyte. Compared to S-850 (0.881 V) and S-850-B (0.805 V), S-850-1 exhibits a higher peak potential (0.895 V), closely matching that of 20% Pt/C (0.899 V). The results show that the N, B dual-doped carbon catalyst has significantly higher ORR performance than the N or B mono doped carbon catalyst, even approaching that of 20% Pt/C. The peak potentials of the N and B mono doped carbon catalysts (S-850 and S-850-B) are higher than those of the N, B dual-doped SN-850-1 (0.795 V) with low surface area and non-porous structure, indicating a direct relationship between surface area, porosity, and ORR performance.

Among the carbon catalysts with different doped O contents, S-1000-2 (O: 5.34 at%) and S-1000-3 (O: 3.21 at%) without N and B doping exhibit similar peak potentials of 0.682 V, which are lower than those of the N- and B-doped carbon catalysts, indicating that O

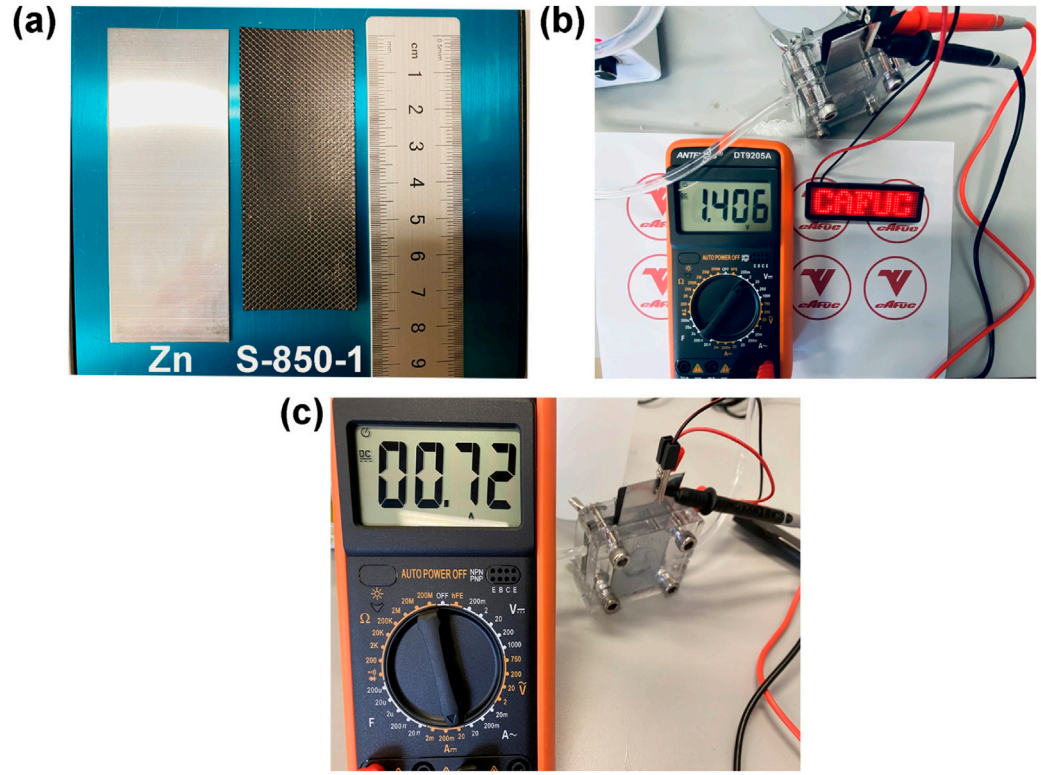

FIGURE 7
(A) S-850-1 and Zn plate, **(B)** Open circuit voltage, **(C)** Current density of Zn-air battery.

doping has a minimal effect on ORR performance. Furthermore, the peak potential of the most effective S-850-1 exceeds that of previously reported N and B dual-doped carbon catalysts (BN-GNRs: 0.870 V (Tu et al., 2022), B-NHMC: 0.881 V (Al-Enizi, 2022), BNC-600: 0.759 V (Zhou et al., 2021)), which can be attributed to its lower N and B content, as well as its smaller surface area and pore structure. The LSV curves, shown in Figure 5B, demonstrate that the performance of S-850-1 is like that of 20% Pt/C. Specifically, S-850-1 shows improvements of 23 mV and 0.36 mA cm^{-2} in half-wave potential and limited current density (0.861 V and −5.60 mA cm^{-2}), respectively, compared to S-850 (0.838 V and −5.24 mA cm^{-2}). The half-wave potential and limited current density of S-850-1 are nearly identical to those of 20% Pt/C. While S-850-1 starts with an initial potential of 0.962 V, it shifts negatively by 83 mV compared to the 1.050 V of 20% Pt/C. The trends observed in the onset potential, half-wave potential, and limited diffusion current density of the other samples are consistent with the above CV results. The detailed electrochemical data are listed in Table 1.

Based on the preceding physical and electrochemical test results, the N, B dual-doped carbon structure demonstrates a notable enhancement in ORR performance, surpassing that of the mono N and B doped carbon structures. Furthermore, the ORR activity of the N, B dual-doped carbon catalyst S-850-1 exceeds that of previously reported N, B dual-doped materials in the literature, suggesting that S-850-1 holds substantial potential for commercialization as an ORR catalyst. The LSV curves (rotation rates: 400–2,500 rpm), shown in Figure 5C, demonstrate that higher rotation rates increase the limiting diffusion current density, reduce diffusion distance, and enhance oxygen transport (Tan et al., 2012). K-L plots within the 0.3–0.7 V potential range reveal strong linearity for S-850-1, suggesting first-order reaction kinetics for oxygen reduction (Xu et al., 2017). Moreover, S-850-1 has an electron transfer number (n) of 3.85, indicating a predominant 4-electron ORR way.

The longevity of catalysts is a key challenge for fuel cell commercialization (Wu et al., 2011). After 5,000 CV cycles, S-850-1 shows a negative shift of 26 mV in half-wave potential (@1,600 rpm) and a decrease of −0.52 mA cm^{-2} in limiting diffusion current density from its initial values. In comparison, commercial 20% Pt/C experiences a more significant decline, with shifts of 161 mV and −1.64 mA cm^{-2}, respectively (Figure 6A). The outstanding stability of S-850-1 may be ascribed to the robust covalent C-N bonds and the lack of complications such as Pt nanoparticle aggregation and dissolution (Zhong et al., 2013). Additionally, under chronoamperometric testing at 0.5 V for 18,000 s, the current density of 20% Pt/C drops to 0.8 mA cm^{-2}, while S-850-1 maintains a current density of approximately 1.1 mA cm^{-2} (Figure 6B). CO gas poses a significant challenge for fuel cells by increasing the risk of ORR catalyst poisoning. Figure 6C illustrates the catalysts' tolerance to CO. Upon CO introduction at 4,000 s, 20% Pt/C's current density decreases to about 56%, indicating a higher susceptibility to CO poisoning compared to S-850-1, which retains about 79% of its current density. In direct methanol fuel cells, methanol may migrate from the anode to the cathode, where it can potentially poison the ORR catalyst (Gao et al., 2015c). Therefore, methanol tolerance

is crucial for optimal catalyst performance. As shown in Figure 6D, S-850-1 demonstrates high selectivity for oxygen and shows no significant activity loss upon the addition of 10 mL methanol, indicating effective resistance to methanol crossover. In contrast, the ORR performance of 20% Pt/C is adversely affected by methanol, as it is more prone to methanol oxidation reactions (MOR). These results highlight that S-850-1 surpasses 20% Pt/C in terms of stability and resistance to methanol and CO poisoning.

This study constructs a Zn-air battery to further investigate the performance of S-850-1. The Zn-air battery features a 4.5 cm^2 operating surface, with a 6 M KOH solution circulating at 20 mL per minute as the electrolyte. The oxide layer is removed by sanding the zinc plate (length: about 8.5 cm, width: about 3 cm), as shown in Figure 7A. S-850-1 coated on stainless steel mesh (approximate length: 7.5 cm, approximate width: 3 cm). The Zn-air battery's open circuit voltage and current density in Figure 7B, c are 1.40 V and 0.72 A, respectively, which illuminates the LED light. The findings suggest that S-850-1 may be used as an ORR catalyst for Zn-air batteries.

Future research directions will focus on exploring novel biomass that is inherently rich in various heteroatoms, enabling the formation of self-doped carbon-based ORR catalysts with high heteroatom content. This approach will avoid the use of external doping chemicals and reduce preparation costs. In the process of scaling up the industrial production of biomass-derived carbon-based ORR catalysts, challenges may arise due to variations in the heteroatom content caused by differences in the origin and seasonal changes of biomass materials across different batches. Additionally, it is crucial to develop scalable and cost-effective processes, such as ball milling, to produce heteroatom-doped carbon-based electrocatalysts. These processes should ensure the catalysts possess optimal structural and surface chemical properties to meet the demands of industrial applications (Sekhon et al., 2022; Koolen et al., 2023).

4 Conclusion

The study successfully develops an efficient N, B dual-doped carbon ORR catalyst (S-850-1) using Saccharina japonica, DFT calculations, $NaBH_4$ doping, and pyrolysis methods. Initially, six theoretical models demonstrate that N and B dual-doping carbon offers superior ORR performance compared to N and B mono-doped carbon. Saccharina japonica and $NaBH_4$ serve as the precursor and boron source, respectively, for pyrolyzing N (4.54 at%) and B (1.05 at%) dual-doped carbon (S-850-1) at 850°C. The ORR activity of S-850-1 outperforms that of N mono-doped carbon (S-850), evidenced by its higher half-wave potential (0.861 vs. 0.838 V) and greater limited current density (−5.60 vs. −5.24 mA cm^{-2}). This indicates that N, B dual-doping carbon has enhanced ORR performance. Furthermore, S-850-1 is utilized to fabricate a Zn-air battery with an open circuit voltage of 1.40 V, successfully powering an LED light. These electrochemical results corroborate the DFT predictions, suggesting that S-850-1, derived from the widely available Saccharina japonica, has the potential to be a commercially viable ORR catalyst for the next generation of fuel cells.

Data availability statement

The original contributions presented in the study are included in the article/supplementary material, further inquiries can be directed to the corresponding authors.

Author contributions

JZ: Writing–original draft, Writing–review and editing. CW: Writing–original draft, Writing–review and editing. JW: Writing–review and editing. MX: Writing–review and editing. SL: Writing–review and editing. LL: Writing–review and editing. WW: Writing–review and editing. XP: Writing–review and editing.

Funding

The author(s) declare that financial support was received for the research, authorship, and/or publication of this article. Fundamental Research Funds for the Central Universities (No. 24CAFUC04004, 24CAFUC03028), National Natural Science Foundation of China (No. 52205238, 12304258), Natural Science Foundation of Sichuan Province (No. 2022NSFSC1894, No. 2022NSFSC1885), the Joint Fund Project supported by the National Nature Science Foundation of China and the Civil Aviation Administration of China (No. U2133209), the Fundamental Research Funds for the Central Universities (No. J2022-005).

Conflict of interest

The authors declare that the research was conducted in the absence of any commercial or financial relationships that could be construed as a potential conflict of interest.

Publisher's note

All claims expressed in this article are solely those of the authors and do not necessarily represent those of their affiliated organizations, or those of the publisher, the editors and the reviewers. Any product that may be evaluated in this article, or claim that may be made by its manufacturer, is not guaranteed or endorsed by the publisher.

References

Alatalo, S. M., Qiu, K. P., Preuss, K., Marinovic, A., Sevilla, M., Sillanpaa, M., et al. (2016). Soy protein directed hydrothermal synthesis of porous carbon aerogels for electrocatalytic oxygen reduction. *Carbon* 96, 622–630. doi:10.1016/j.carbon.2015.09.108

Al-Enizi, A. M. (2022). Waste cigarette butt-derived B, N doped bifunctional hierarchical mesoporous carbon for supercapacitor and oxygen reduction reaction. *Colloids Surfaces a-Physicochemical Eng. Aspects* 643, 128775. doi:10.1016/j.colsurfa.2022.128775

Arif, M., Mahsud, A., Muhmood, T., and Deepak, F. L. (2024). Design, synthesis, and electronic structure modulation of ORR electrocatalysts. *J. Environ. Chem. Eng.* 12, 113417. doi:10.1016/j.jece.2024.113417

Bhoyate, S. D., Kim, J., de Souza, F. M., Lin, J. R. Y., Lee, E. H., Kumar, A., et al. (2023). Science and engineering for non-noble-metal-based electrocatalysts to boost their ORR performance: a critical review. *Coord. Chem. Rev.* 474, 214854. doi:10.1016/j.ccr.2022.214854

Borghei, M., Lehtonen, J., Liu, L., and Rojas, O. J. (2018). Advanced biomass-derived electrocatalysts for the oxygen reduction reaction. *Adv. Mat.* 30, 1703691. doi:10.1002/adma.201703691

Cai, X. Y., Lai, L. F., Zhou, L. J., and Shen, Z. X. (2019). Durable freestanding hierarchical porous electrode for rechargeable zinc-air batteries. *Acs Appl. Energy Mater.* 2, 1505–1516. doi:10.1021/acsaem.8b02101

Chen, P., Wang, L. K., Wang, G., Gao, M. R., Ge, J., Yuan, W. J., et al. (2014). Nitrogen-doped nanoporous carbon nanosheets derived from plant biomass: an efficient catalyst for oxygen reduction reaction. *Energy and Environ. Sci.* 7, 4095–4103. doi:10.1039/c4ee02531h

Choi, C. H., Chung, M. W., Kwon, H. C., Park, S. H., and Woo, S. I. (2013). B, N- and P, N-doped graphene as highly active catalysts for oxygen reduction reactions in acidic media. *J. Mat. Chem. A* 1, 3694–3699. doi:10.1039/c3ta01648j

Choi, C. H., Park, S. H., and Woo, S. I. (2012). Phosphorus-nitrogen dual doped carbon as an effective catalyst for oxygen reduction reaction in acidic media: effects of the amount of P-doping on the physical and electrochemical properties of carbon. *J. Mat. Chem.* 22, 12107–12115. doi:10.1039/c2jm31079a

Ferrero, G. A., Fuertes, A. B., Sevilla, M., and Titirici, M. M. (2016). Efficient metal-free N-doped mesoporous carbon catalysts for ORR by a template-free approach. *Carbon* 106, 179–187. doi:10.1016/j.carbon.2016.04.080

Gao, S. Y., Chen, Y. L., Fan, H., Wei, X. J., Hu, C. G., Wang, L. X., et al. (2014a). A green one-arrow-two-hawks strategy for nitrogen-doped carbon dots as fluorescent ink and oxygen reduction electrocatalysts. *J. Mater. Chem. A* 2, 6320–6325. doi:10.1039/c3ta15443b

Gao, S. Y., Fan, H., and Zhang, S. X. (2014b). Nitrogen-enriched carbon from bamboo fungus with superior oxygen reduction reaction activity. *J. Mater. Chem. A* 2, 18263–18270. doi:10.1039/c4ta03558e

Gao, S. Y., Li, L. Y., Geng, K. R., Wei, X. J., and Zhang, S. X. (2015a). Recycling the biowaste to produce nitrogen and sulfur self-doped porous carbon as an efficient catalyst for oxygen reduction reaction. *Nano Energy* 16, 408–418. doi:10.1016/j.nanoen.2015.07.009

Gao, S. Y., Liu, H. Y., Geng, K. R., and Wei, X. J. (2015b). Honeysuckles-derived porous nitrogen, sulfur, dual-doped carbon as high-performance metal-free oxygen electroreduction catalyst. *Nano Energy* 12, 785–793. doi:10.1016/j.nanoen.2015.02.004

Gao, S. Y., Wei, X. J., Liu, H. Y., Geng, K., Wang, H. Q., Moehwald, H., et al. (2015c). Transformation of worst weed into N-S-and P-tridoped carbon nanorings as metal-free electrocatalysts for the oxygen reduction reaction. *J. Mater. Chem. A* 3, 23376–23384. doi:10.1039/c5ta04809e

Gu, D. G., Zhou, Y., Ma, R. G., Wang, F. F., Liu, Q., and Wang, J. C. (2018). Facile synthesis of N-doped graphene-like carbon nanoflakes as efficient and stable electrocatalysts for the oxygen reduction reaction. *Nano-Micro Lett.* 10, 29–12. doi:10.1007/s40820-017-0181-1

Guo, C. Z., Liao, W. L., Li, Z. B., Sun, L. T., and Chen, C. G. (2015). Easy conversion of protein-rich enki mushroom biomass to a nitrogen-doped carbon nanomaterial as a promising metal-free catalyst for oxygen reduction reaction. *Nanoscale* 7, 15990–15998. doi:10.1039/c5nr03828f

Guo, J. H., Zhang, S. L., Zheng, M. X., Tang, J., Liu, L., Chen, J. M., et al. (2020). Graphitic-N-rich N-doped graphene as a high performance catalyst for oxygen reduction reaction in alkaline solution. *Int. J. Hydrogen Energy* 45, 32402–32412. doi:10.1016/j.ijhydene.2020.08.210

Higgins, D. C., Hoque, M. A., Hassan, F., Choi, J. Y., Kim, B., and Chen, Z. W. (2014). Oxygen reduction on graphene-carbon nanotube composites doped sequentially with nitrogen and sulfur. *ACS Catal.* 4, 2734–2740. doi:10.1021/cs5003806

Hren, M., Bozic, M., Fakin, D., Kleinschek, K. S., and Gorgieva, S. (2021). Alkaline membrane fuel cells: anion exchange membranes and fuels. *Sustain. Energy and Fuels* 5, 604–637. doi:10.1039/d0se01373k

Huang, N. B., Zhang, J. J., Sun, Y., Sun, X. N., Qiu, Z. Y., and Ge, X. W. (2020). A non-traditional biomass-derived N, P, and S ternary self-doped 3D multichannel carbon ORR electrocatalyst. *New J. Chem.* 44, 14604–14614. doi:10.1039/d0nj03283b

Huang, X. B., Wang, Q., Jiang, D., and Huang, Y. M. (2017). Facile synthesis of B, N co-doped three-dimensional porous graphitic carbon toward oxygen reduction reaction and oxygen evolution reaction. *Catal. Commun.* 100, 89–92. doi:10.1016/j.catcom.2017.06.045

Huang, Z., Ruan, H. B., Zhang, H., Shi, D. P., Li, W. J., Qin, G. P., et al. (2019). Conversion mechanism of conductivity and properties of nitrogen implanted ZnO single crystals induced by post-annealing. *J. Mater. Science-Materials Electron.* 30, 4555–4561. doi:10.1007/s10854-019-00745-y

Kim, H., Cho, J., Jang, S. Y., and Song, Y. W. (2011). Deformation-immunized optical deposition of graphene for ultrafast pulsed lasers. *Appl. Phys. Lett.* 98, 021104. doi:10.1063/1.3536502

Koolen, C. D., Luo, W., and Züttel, A. (2023). From single crystal to single atom catalysts: structural factors influencing the performance of metal catalysts for CO2 electroreduction. *Acs Catal.* 13, 948–973. doi:10.1021/acscatal.2c03842

Lee, W., Kim, G. M., Baik, S., and Lee, J. W. (2016). Carbon dioxide conversion into boron/nitrogen dual-doped carbon as an electrode material for oxygen reduction reaction. *Electrochimica Acta* 210, 743–753. doi:10.1016/j.electacta.2016.05.206

Li, Y. H., Qu, Y. J., Liu, C. C., Cui, J. D., Xu, K., Li, Y., et al. (2022). Processing agricultural cornstalks toward high-efficient stable bifunctional ORR/OER electrocatalysts. *Adv. Sustain. Syst.* 6, 2100343. doi:10.1002/adsu.202100343

Li, Z. T., Liu, D. M., Cai, Y. D., Wang, Y. P., and Teng, J. (2019). Adsorption pore structure and its fractal characteristics of coals by N2 adsorption/desorption and FESEM image analyses. *Fuel* 257, 116031. doi:10.1016/j.fuel.2019.116031

Liang, J. Y., and Yuan, Q. H. (2024). Effects of graphitic- and pyridinic-N co-doping on structure regulation and ORR activity of N-doped graphene. *Appl. Surf. Sci.* 648, 159025. doi:10.1016/j.apsusc.2023.159025

Liu, D. T., Qian, Z. Y., Li, Y. H., Luo, Y., Liu, C. C., and Cui, J. D. (2024). N, B, F - engineered nanocellulose - cornstalks aerogels for high-performance ORR/OER materials. *Adv. Sustain. Syst.* 8, 2300594. doi:10.1002/adsu.202300594

Liu, F. F., Peng, H. L., You, C. H., Fu, Z. Y., Huang, P. Y., Song, H. Y., et al. (2014). High-performance doped carbon catalyst derived from nori biomass with melamine promoter. *Electrochimica Acta* 138, 353–359. doi:10.1016/j.electacta.2014.06.098

Liu, X. J., Zhou, Y. C., Zhou, W. J., Li, L. G., Huang, S. B., and Chen, S. W. (2015). Biomass-derived nitrogen self-doped porous carbon as effective metal-free catalysts for oxygen reduction reaction. *Nanoscale* 7, 6136–6142. doi:10.1039/c5nr00013k

Mao, Z. X., Tang, X. Y., An, X. G., and Jiang, J. X. (2022). Defective nanomaterials for electrocatalysis oxygen reduction reaction. *Front. Chem.* 10, 1023617–1023619. doi:10.3389/fchem.2022.1023617

Sekhon, S. S., Lee, J., and Park, J. S. (2022). Biomass-derived bifunctional electrocatalysts for oxygen reduction and evolution reaction: a review. *J. Energy Chem.* 65, 149–172. doi:10.1016/j.jechem.2021.05.052

Su, D. D., Xiang, W., Liang, Q., Wen, L., Shi, Y., Song, B. Q., et al. (2022). Tomato SlBES1.8 influences leaf morphogenesis by mediating gibberellin metabolism and signaling. *Plant Cell. Physiology* 63, 535–549. doi:10.1093/pcp/pcac019

Su, Z. W., Liu, X. N., Hao, S. Y., Li, Z. J., Yang, B., Hou, Y., et al. (2021). Pt/CoFe2O4-C hollow ball as efficient bifunctional electrocatalyst for Zn-air batteries. *Catal. Today* 368, 204–210. doi:10.1016/j.cattod.2020.04.015

Tan, Y. M., Xu, C. F., Chen, G. X., Fang, X. L., Zheng, N. F., and Xie, Q. J. (2012). Facile synthesis of manganese-oxide-containing mesoporous nitrogen-doped carbon for efficient oxygen reduction. *Adv. Funct. Mat.* 22, 4584–4591. doi:10.1002/adfm.201201244

Tu, H. L., Zhang, Y. M., Liu, P. Z., Hou, Y., Liu, Y. Z., Liang, J. G., et al. (2022). B, N co-doping graphene nanoribbons as effective oxygen reduction electrocatalyst. *Mater. Res. Express* 9, 115603. doi:10.1088/2053-1591/ac9fae

Wang, M., Wang, S. Y., Yang, H. Q., Ku, W., Yang, S. C., Liu, Z. N., et al. (2020). Carbon-based electrocatalysts derived from biomass for oxygen reduction reaction: a minireview. *Front. Chem.* 8, 116–212. doi:10.3389/fchem.2020.00116

Wang, S. Y., Yu, D. S., Dai, L. M., Chang, D. W., and Baek, J. B. (2011). Polyelectrolyte-functionalized graphene as metal-free electrocatalysts for oxygen reduction. *ACS Nano* 5, 6202–6209. doi:10.1021/nn200879h

Wei, P., Li, X. G., He, Z. M., Sun, X. P., Liang, Q. R., Wang, Z. Y., et al. (2021). Porous N, B co-doped carbon nanotubes as efficient metal-free electrocatalysts for ORR and Zn-air batteries. *Chem. Eng. J.* 422, 130134. doi:10.1016/j.cej.2021.130134

Wu, G., More, K. L., Johnston, C. M., and Zelenay, P. (2011). High-performance electrocatalysts for oxygen reduction derived from polyaniline, iron, and cobalt. *Science* 332, 443–447. doi:10.1126/science.1200832

Xiao, F., Wang, Y. C., Wu, Z. P., Chen, G. Y., Yang, F., Zhu, S. Q., et al. (2021). Recent advances in electrocatalysts for proton exchange membrane fuel cells and alkaline membrane fuel cells. *Adv. Mater.* 33, 2006292. doi:10.1002/adma.202006292

Xu, L. N., Fan, H., Huang, L. X., Xia, J. L., Li, S. H., Li, M., et al. (2017). Chrysanthemum-derived N and S co-doped porous carbon for efficient oxygen reduction reaction and aluminum-air battery. *Electrochimica Acta* 239, 1–9. doi:10.1016/j.electacta.2017.04.002

Xu, X., Kim, J. Y., Oh, Y. R., and Park, J. M. (2014). Production of biodiesel from carbon sources of macroalgae, Laminaria japonica. *Bioresour. Technol.* 169, 455–461. doi:10.1016/j.biortech.2014.07.015

Yang, S. B., Zhi, L. J., Tang, K., Feng, X. L., Maier, J., and Mullen, K. (2012). Efficient synthesis of heteroatom (N or S)-Doped graphene based on ultrathin graphene oxide-porous silica sheets for oxygen reduction reactions. *Adv. Funct. Mat.* 22, 3634–3640. doi:10.1002/adfm.201200186

Yu, H. T., Li, Y. C., Li, X. H., Fan, L. Z., and Yang, S. H. (2014). Electrochemical preparation of N-doped cobalt oxide nanoparticles with high electrocatalytic activity for the oxygen-reduction reaction. *Chem.-Eur. J.* 20, 3457–3462. doi:10.1002/chem.201303814

Zeng, K., Su, J. M., Cao, X. C., Zheng, X. J., Li, X. W., Tian, J. H., et al. (2020). B, N Co-Doped ordered mesoporous carbon with enhanced electrocatalytic activity for the oxygen reduction reaction. *J. Alloys Compd.* 824, 153908. doi:10.1016/j.jallcom.2020.153908

Zhang, J., Pham, T. H., Gao, Z. X., Li, M., Ko, Y. D., Lombardo, L., et al. (2023b). Electrochemical CO2 reduction over copper phthalocyanine derived catalysts with enhanced selectivity for multicarbon products. *Acs Catal.* 13, 9326–9335. doi:10.1021/acscatal.3c01439

Zhang, J. J., Xing, P., Wei, W. G., Qiu, C., and Sun, X. L. (2023a). DFT-guided design and synthesis of sea cucumber-derived N, S dual-doped porous carbon catalyst for enhanced oxygen reduction reaction and Zn-air battery performance. *J. Mater. Sci.* 58, 11968–11981. doi:10.1007/s10853-023-08781-0

Zhao, C. J., Liu, G. Q., Sun, N., Zhang, X., Wang, G. Z., Zhang, Y. X., et al. (2018). Biomass-derived N-doped porous carbon as electrode materials for Zn-air battery powered capacitive deionization. *Chem. Eng. J.* 334, 1270–1280. doi:10.1016/j.cej.2017.11.069

Zhao, Q., Yan, Z. H., Chen, C. C., and Chen, J. (2017). Spinels: controlled preparation, oxygen reduction/evolution reaction application, and beyond. *Chem. Rev.* 117, 10121–10211. doi:10.1021/acs.chemrev.7b00051

Zheng, Y., Liu, J., Liang, J., Jaroniec, M., and Qiao, S. Z. (2012). Graphitic carbon nitride materials: controllable synthesis and applications in fuel cells and photocatalysis. *Energy Environ. Sci.* 5, 6717–6731. doi:10.1039/c2ee03479d

Zhong, H. X., Zhang, H. M., Liu, S. S., Deng, C. W., and Wang, M. R. (2013). Nitrogen-Enriched carbon from melamine resins with superior oxygen reduction reaction activity. *ChemSusChem* 6, 807–812. doi:10.1002/cssc.201200919

Zhou, S. Y., Zang, J. B., Li, W., Tian, P. F., Gao, H. W., Song, S. W., et al. (2021). B, N Co-doped nanocarbon derived *in situ* from nanoboron carbide as electrocatalyst for oxygen reduction reaction. *Chemnanomat* 7, 200–206. doi:10.1002/cnma.202000613